

A JET-DRIVEN, EXTREME HIGH-VELOCITY OUTFLOW POWERED BY A COLD, LOW-LUMINOSITY PROTOSTAR NEAR NGC 2023

G. SANDELL,¹ L. W. AVERY,² F. BAAS,³ I. COULSON,³ W. R. F. DENT,⁴ P. FRIBERG,³ W. P. K. GEAR,⁵ J. GREAVES,³ W. HOLLAND,³ T. JENNESS,³ P. JEWELL,¹ J. LIGHTFOOT,⁴ H. E. MATTHEWS,³ G. MORIARTY-SCHIEVEN,³ R. PRESTAGE,³ E. I. ROBSON,³ J. STEVENS,⁵ R. P. J. TILANUS,³ AND G. D. WATT³

Received 1998 October 23; accepted 1999 February 8

ABSTRACT

We have discovered an extreme high-velocity bipolar CO outflow in the vicinity of NGC 2023, with total outflow velocities of $\sim 200 \text{ km s}^{-1}$. At very high velocities this outflow is jetlike with an opening angle $\leq 4^\circ$, while it shows a separate outflow lobe at low velocities. The outflow is bipolar and exhibits a clear mirror symmetry, which suggests that the source powering the outflow is episodic or precessing. The dynamical timescales for the outflow are $\leq 3000 \text{ yr}$. We identify the source driving the CO jet with a deeply embedded low-luminosity submillimeter double source (separation $\sim 23''$), where the primary component lies on the symmetry axis of the outflow and has all the signatures of a “class 0” protostellar object. Analysis of molecular data and (sub)millimeter photometry suggests that the driving source is cold and compact, with a luminosity of $\lesssim 10 L_\odot$ and a total mass of $1.8\text{--}4.6 M_\odot$. It has no near-IR counterpart, it drives an extremely young outflow, and it emits a large fraction of its luminosity in the submillimeter regime. Both millimeter sources have low dust emissivity, $\beta \sim 0.8\text{--}1.3$, similar to what is found for other class 0 objects, while the surrounding molecular cloud core appears to have a $\beta \sim 2.0$, the canonical value for “normal” interstellar dust in the submillimeter regime.

Subject headings: ISM: individual (NGC 2023) — ISM: jets and outflows — ISM: molecules — stars: pre-main-sequence

1. INTRODUCTION

The common understanding of star formation is that stars form from collapsing cloud cores in molecular clouds. Yet, there is hardly any direct observational evidence of accretion in young stars and “protostellar” candidates. A far more commonly observed property in young stars is outflow, not infall, which is most commonly seen as molecular outflows. These bipolar outflows are believed to be driven by strong stellar winds or jets, fed by accretion activity. Currently there are more than 200 known molecular outflows, the majority of which show moderate outflow velocities, i.e., about $10\text{--}30 \text{ km s}^{-1}$. A small subset of outflows, called extreme high-velocity (EHV) outflows, show outflow velocities of about 100 km s^{-1} or more (Choi, Evans, & Jaffe 1993).

While mapping the Horsehead Nebula and the surrounding molecular cloud in CO $J = 2 \rightarrow 1$ with the James Clerk

Maxwell Telescope (JCMT)⁶ on Mauna Kea, we found an extreme high-velocity outflow northeast of the Horsehead Nebula, in the vicinity of NGC 2023. This outflow is driven by a deeply embedded submillimeter source and clearly belongs to the EHV outflow group. The outflow is very intense and easily detectable even with short integration times. Other prominent features of the outflow are that it is extremely well-collimated and that the red- and the blue-shifted lobes exhibit a mirror symmetry, which suggests that the outflow activity is either episodic or precessing or both.

In this paper we discuss the unique properties of this outflow and the associated submillimeter source and demonstrate that it should be added to the growing number of young protostellar “class 0” objects.

2. OBSERVATIONS

2.1. Molecular Line Observations

The NGC 2023 outflow was discovered while mapping the Horsehead Nebula and the surrounding molecular cloud in CO $J = 2 \rightarrow 1$ as a general JCMT poor weather backup (Sandell 1999). The CO $J = 2 \rightarrow 1$ data presented in this paper are a small subset of the Horsehead data and were done in on-the-fly mode using the DAS (Digital Autocorrelator Spectrometer) and RxA2, our 230 GHz SIS receiver in rather marginal weather conditions with integration times of 5 s per point. To help maintain relative night-to-night calibration with $\sim 5\%$, our observing procedure involved significant overlap of rasters and well as some repetition of the mapped regions. The velocity resolution and coverage were ~ 0.1 and 200 km s^{-1} . The rms noise in the map is $\sim 0.4 \text{ K}$ per channel.

⁶ The James Clerk Maxwell Telescope is operated on a joint basis between the United Kingdom Particle Physics and Astronomy Research Council (PPARC), the Netherlands Organisation for the Advancement of Pure Research (ZWO), the Canadian National Research Council (NRC), and the University of Hawaii (UH).

¹ National Radio Astronomy Observatory, P.O. Box 2, Green Bank, WV 24944; gsandell@nrao.edu, pjewell@jach.hawaii.edu. The NRAO is a facility of the National Science Foundation operated under cooperative agreement by Associated Universities, Inc.

² National Research Council, Herzberg Institute of Astrophysics, 5071 W. Saanich Road., Victoria, BC V8X 4M6, Canada; lorne.avery@hia.nrc.ca.

³ Joint Astronomy Centre, 660 North A’Ohōkū Place, Hilo, HI 96720; f.baas@jach.hawaii.edu, i.coulson@jach.hawaii.edu, p.friberg@jach.hawaii.edu, j.greaves@jach.hawaii.edu, w.holland@jach.hawaii.edu, t.jenness@jach.hawaii.edu, h.matthews@jach.hawaii.edu, g.moriarty-schieven@jach.hawaii.edu, r.prestage@jach.hawaii.edu, i.robson@jach.hawaii.edu, r.tilanus@jach.hawaii.edu, g.watt@jach.hawaii.edu.

⁴ Astronomy Technology Centre, Edinburgh, Blackford Hill, Edinburgh EH9 3HJ, Scotland, UK; W.Dent@roe.ac.uk, J.Lightfoot@roe.ac.uk.

⁵ Mullard Space Science Laboratory, Holmbury, St. Mary, Dorking, Surrey RH5 6NT UK; wkp@msl.ac.uk, jas@msl.ac.uk.

TABLE 1
CONTINUUM DATA OF NGC 2023 mm1 AND mm2

Filter/HPBW	Flux (mm1) (Jy beam ⁻¹)	Flux (mm2) (Jy beam ⁻¹)
2.0 mm/27"	0.63 ± 0.08 (1)	...
1.3 mm/19"5	1.26 ± 0.11 (1)	...
1.3 mm/12"0 ^a	1.12	0.30
1.1 mm/18"5	1.55 ± 0.15 (4)	0.6
850 μm/14"6	2.6 ± 0.3	1.1 ± 0.2 ^b
800 μm/16"5	3.68 ± 0.25 (3)	...
800 μm/13"5	3.55 ± 0.3 (2)	1.75
450 μm/18"	15.8 ± 1.8 (2)	...
450 μm/8"6	6.6 ± 2.0	1.9 ± 0.6
350 μm/19"	26.7 ± 5.0 (2)	...

NOTE.—The numbers in parenthesis refer to the numbers of independent photometry observations. The 850 and 450 μm SCUBA data are from maps and give the peak flux from Gaussian fits with background emission subtracted, see text. All data on mm2 are derived from maps.

^a Results from Launhardt et al. 1996

^b Difficult to fit a Gaussian. The fit used gives FWHM of 23"3 × 17"6, whereas 450 μm data suggest a deconvolved size of ~ 10".

We have also obtained a CO $J = 3 \rightarrow 2$ map of the same field with some long integration spectra in CO $J = 3 \rightarrow 2$, CO $J = 2 \rightarrow 1$, and ¹³CO $J = 2 \rightarrow 1$ of selected positions in the outflow, as well as some additional molecular observations of the central source.

The CO $J = 3 \rightarrow 2$ map was obtained in the same way as the CO $J = 2 \rightarrow 1$ map, i.e., as an on-the-fly map using our 300 GHz receivers, RxB3i, and the newly commissioned RxB3, the latter being a single sideband (SSB) receiver. We found no difference in calibration between the two receivers. The noise level in the CO $J = 3 \rightarrow 2$ map is more variable than the CO $J = 2 \rightarrow 1$ map, with the rms noise level varying from 0.4 to 1.2 K per channel. The high noise levels

are mostly in the outskirts of the map; over the actual outflow the rms noise level is ~0.4–0.7 K per channel.

All data are calibrated using three-position chopping, i.e., cold load, hot load, and sky, enabling us to monitor the receiver temperature as well as the sky opacity. The raw spectra are baseline corrected with a linear baseline for CO $J = 2 \rightarrow 1$ and a first- or second-order polynomial for CO $J = 3 \rightarrow 2$. Overlapping data points are noise-weighted co-adds. Final data are given in main beam brightness temperature, T_{mb} . At 230 GHz the half power beamwidth (HPBW) is 21"5, and at 345 GHz the HPBW is ~14". The main beam efficiency, η_{mb} , as determined from planet observations, is 0.68 for RxA2 and 0.58 for RxB3.

2.2. Continuum Photometry and Mapping

The expected position of the exciting source was searched for continuum emission at 800 μm, and we detected strong (3.5 Jy beam⁻¹) emission within our 10" search box. The initial source position was determined by five-point observations offsetting from a strong nearby blazar (0528 + 134). Submillimeter photometry (2 mm–350 μm) with our common user bolometer UKT14 (Duncan et al. 1990) was carried out in the normal way and calibrated using planets and secondary calibrators (Sandell 1994). Results of the (sub)millimeter photometry are presented in Table 1.

We also mapped the source both at 1.1 mm and 800 μm using UKT14 and conventional dual-beam mapping. Both the 1.1 mm and 800 μm maps were taken in relatively poor (high opacity) conditions and do not go very deep. However, both maps clearly show the source to be double.

The source was also used as a test source during commissioning of the Submillimetre Common-User Bolometer Array (SCUBA), and hence we have two rather deep maps at 850 and 450 μm. SCUBA is the new common user submillimeter continuum bolometer array on JCMT. For a description of SCUBA, see (Holland et al. 1998). The SCUBA maps presented here were obtained with 90" and 120" chops and a 64 jiggle pattern and are co-adds of

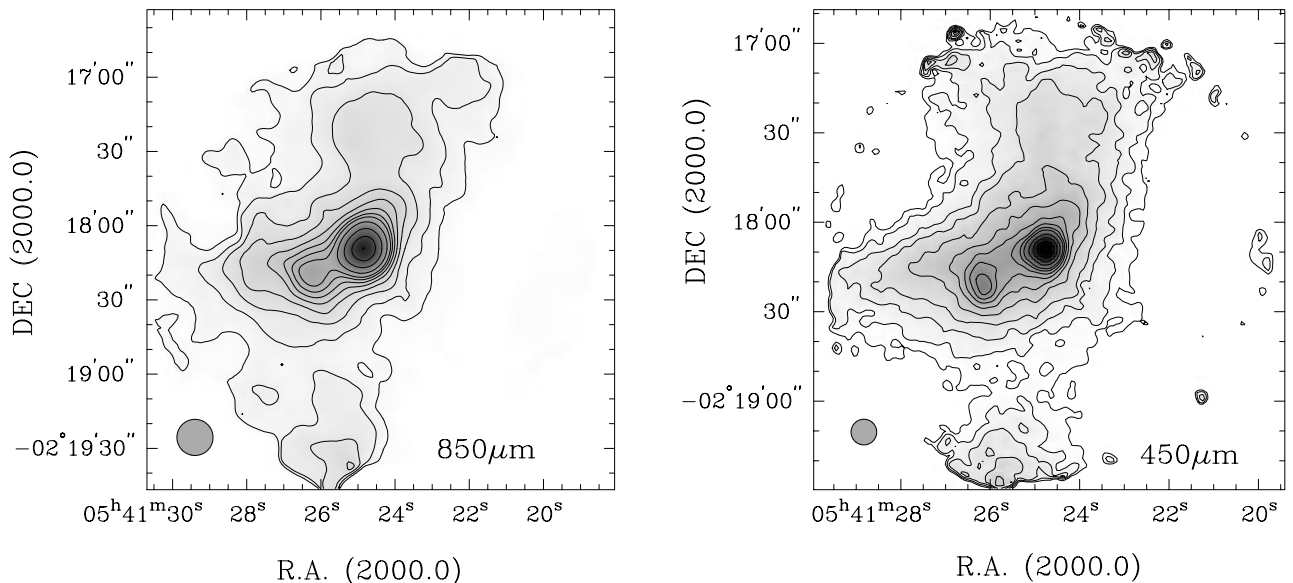


FIG. 1.—Gray-scale 850 and 450 μm continuum maps overlaid with contours of the field surrounding NGC 2023 mm1 and mm2. The lowest contours are at 2.5% of the peak for the 850 μm map and go up in 10% steps, while the lowest contour is at 3% of the peak for the 450 μm map and go up in 10% steps. The SCUBA beam size is indicated in the bottom left-hand corner of each image.

several maps taken at different position angles of the source. The dust emission is clearly more extended than our field of view, because all maps show negative emission features, which result from chopping onto emission in the off positions. Most of the negative features were removed in the data reduction, but the extended emission clearly affects the source morphology at low levels.

The maps have been calibrated using 850 μm skydips to trace the atmospheric opacity and from beam maps of Uranus and Mars obtained during the same night. The 850 μm map is expected to have a calibration accuracy of $\sim 15\%$, while the calibration uncertainty is $\sim 30\%$ at 450 μm . These estimates are based on cross-calibration of Mars and Uranus data. Additional calibration errors are likely to occur, especially at the outskirts of the array, where an unknown amount of extended emission is subtracted from the data. The 850 and 450 μm SCUBA maps are shown in Figure 1.

3. RESULTS AND ANALYSIS

3.1. The Molecular Core

The large CO map of the Horsehead and the adjacent L1630 molecular cloud (Sandell 1999) show a sharp interface between the L1630 dark cloud and the emission nebula IC 434 at velocities $\sim 10.5 \text{ km s}^{-1}$. In the northern part of the map, close to NGC 2023, there is a second large-scale component at $\sim 9.5 \text{ km s}^{-1}$ coexisting with the 10.5 km s^{-1} cloud and largely tracing out the same cloud morphology. The outflow and its associated submillimeter source lie in the outskirts of the L1630 cloud southwest of the bright reflection nebula NGC 2023, $\sim 50''$ east of the sharp molecular cloud boundary toward IC 434.

Launhardt et al. (1996) carried out a 1.3 mm continuum survey of most of the strong CS cores seen by Lada, Bally, & Stark (1991) in the L1630 molecular cloud and detected a double source $120''$ from the nominal center of the core LBS 36, which they labeled LBS 36 SM1 and SM2. This is the same double submillimeter source, which we detected and named NGC 2023 mm1 and mm2, because we find it more closely associated with NGC 2023 than with the CS core. A $\text{C}^{18}\text{O } J=2 \rightarrow 1$ spectrum toward mm1 shows a blended line with velocity components at 9.4 and 10.6 km s^{-1} , while $\text{DCO}^+ J=3-2$ and $\text{H}_2\text{CO } 3_{0,3}-2_{0,2}$ show only the 9.4 km s^{-1} component (Fig. 2). Although the $\text{H}_2\text{CO } 3_{0,3}-2_{0,2}$ line appears to have a second line peak at $\sim 10 \text{ km s}^{-1}$, this “line” is only one channel wide and at a lower velocity than the 10.6 km s^{-1} cloud. This line feature is more likely part of the faint high-velocity pedestal surrounding the 9.4 km s^{-1} component. The $\text{H}_2\text{CO } 3_{2,2}-2_{2,1}$ line, observed simultaneously, shows some of the broad pedestal emission, and very little emission at 9.4 km s^{-1} . The H_2CO line ratio tells us that the 9.4 km s^{-1} cloud is cold, but the S/N ratio of the spectra is not sufficient to constrain the temperature very well, except to say that it is $\leq 40 \text{ K}$. The broad (outflow) component suggests rotational temperatures of $\sim 50 \text{ K}$ or more. From the ratio of the $^{13}\text{CO } J=2 \rightarrow 1$ and $\text{C}^{18}\text{O } J=2 \rightarrow 1$ lines, assuming a $[\text{C}^{18}\text{O}]/[\text{C}^{13}\text{O}]$ abundance ratio of 5.5, we find that $\text{C}^{18}\text{O } J=2 \rightarrow 1$ is moderately optically thick with an optical depth of 0.4 for the 9.4 km s^{-1} cloud and an excitation temperature of 16.5–18.5 K (compact vs. extended emission). The 10.6 km s^{-1} cloud component is also optically thick with $\tau_{\text{C}^{18}\text{O}} \sim 0.5$, but much hotter, $T_{\text{ex}} \sim 39 \text{ K}$. A long integration CO $J=3 \rightarrow 2$ spectrum obtained with

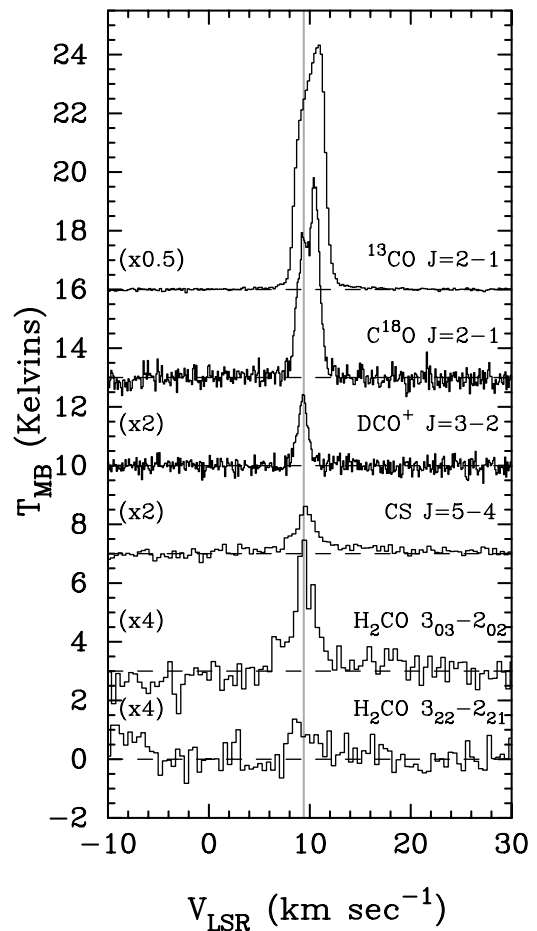


FIG. 2.—Selected spectra toward NGC 2023 mm1 (in T_{mb}). The gray vertical line marks the velocity centroid of the millimeter source. All spectra except $\text{C}^{18}\text{O } J=2 \rightarrow 1$ and $\text{DCO}^+ J=3-2$ show clear wing emission.

RxB3i tuned so that the CS $J=7 \rightarrow 6$ line would appear in the image band shows faint CS emission at velocities of 7.8 km s^{-1} and 6 km s^{-1} Fig. 3. The weak CS $J=7 \rightarrow 6$ emission (or absence of it) from an undoubtedly dense core, is another indication that the cloud core is cold.

In the following we assume that the outflow is associated with the cold 9.4 km s^{-1} cloud core. We base this on inspection of the outflow channel maps and the fact that it is the only core component detected in DCO^+ and H_2CO , both of which trace cold gas at high densities.

3.2. The High-Velocity Outflow

Figure 4 shows the CO $J=3 \rightarrow 2$ outflow at intermediate velocities overlaid on the 850 μm SCUBA image, while Figure 5 shows it integrated over the whole velocity range and rotated by -35° . Next to it we show a position velocity plot and selected long-integration CO $J=2 \rightarrow 1$ spectra of several of the outflow peaks. The total extent of the outflow is somewhat larger in the redshifted lobe than in the blue-shifted one, but on the other hand the outflow velocities are somewhat higher in the red outflow, possibly because the surrounding medium may be more tenuous. At very high velocities the outflow is remarkably jetlike, with a collimation factor (i.e., length/width ratio) greater than 10 or an opening angle of $\leq 4^\circ$. The total extent of the jet is $\sim 160''$ in redshifted CO and $\sim 130''$ in blue, and the maximum velocities are ~ 55 and 45 km s^{-1} for the red and the blue

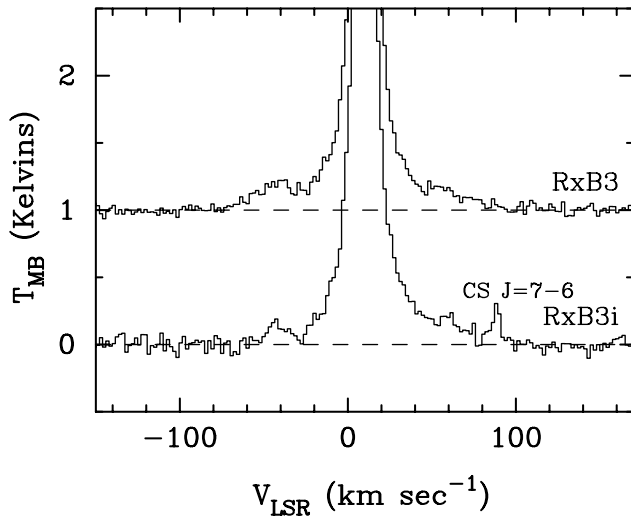


FIG. 3.—Long-integration CO $J = 3 \rightarrow 2$ spectra of NGC 2023 mm1 obtained with RxB3i and RxB3. The spectrum labeled RxB3i was obtained in DSB mode with CS $J = 7 \rightarrow 6$ in the image band. This spectrum was obtained by position switching $800''$ west in R.A. and showed a clear baseline ripple, which was removed by a fifth-order polynomial. The RxB3 spectrum was obtained by beam switching $\pm 60''$ orthogonal to the outflow and had a flat baseline. The total velocity extent is $\sim 80 \text{ km s}^{-1}$ and 120 km s^{-1} in the blue- and redshifted wings, respectively, assuming an ambient cloud velocity of 9.4 km s^{-1} .

outflow, respectively, as determined from long-integration CO $J = 2 \rightarrow 1$ observations of selected positions in the blue and the red outflow. The long-integration CO $J = 3 \rightarrow 2$ spectra (one position-switched, one beam-switched) show that the maximum velocities of the outflow are even higher, $\sim 90 \text{ km s}^{-1}$ in the blueshifted wing and $\sim 110 \text{ km s}^{-1}$ in the redshifted wing (Fig. 3). The CO jet shows three bright regions or hot spots on the red side with corresponding counterparts in the blue, except for the working surface of the jet, which is more pronounced on the redshifted side. The jets are not completely straight, but make several

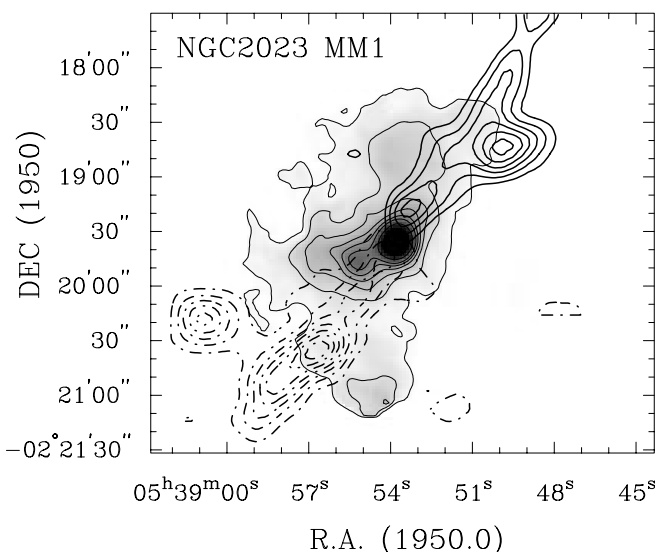


FIG. 4.—Overlay of high-velocity blue- and redshifted CO $J = 3 \rightarrow 2$ emission on the $850 \mu\text{m}$ SCUBA continuum image. The blueshifted emission, plotted with dash-dot contours, is integrated from -15 to 0 km s^{-1} , and the redshifted emission, plotted with solid contours, is integrated from 20 – 40 km s^{-1} .

bends, which are seen in both lobes. At low velocities, especially on the blue side, the outflow appears to split up into a second lobe (labeled be in Fig. 5) $\sim 100''$ from the beginning of the flow. The same is also seen in the red outflow, although it is less pronounced at approximately the same distance from the source.

We also obtained two long-integration $^{13}\text{CO } J = 2 \rightarrow 1$ spectra of the outflow, one toward the center and one in the blue lobe, at an offset (R.A., decl.) = $(40'', -55'')$, i.e., position b2 in Figure 5. If we assume LTE conditions and a ^{12}CO to ^{13}CO ratio of 73 (Choi et al. 1993), we find a ^{12}CO optical depth of ~ 4 – 5 at velocities of 3 km s^{-1} from the line center and $\tau \sim 1$ for outflow velocities of 10 km s^{-1} . These optical depths are similar for both blue and red, but better determined for the blue outflow, because there we have two ^{13}CO spectra. Even though we have long-integration spectra in both CO $J = 2 \rightarrow 1$ and CO $J = 3 \rightarrow 2$ at the center position, we find it difficult to determine accurately the excitation temperature of the high-velocity gas, because of the difference in beam size used for the observations. Neither is the S/N ratio in our maps really sufficient to constrain the temperature accurately at high velocities, where we can assume the gas to be optically thin. The ratio of the integrated line intensities of CO $J = 3 \rightarrow 2$ to CO $J = 2 \rightarrow 1$ over the whole outflow support an excitation temperature, $T_{\text{ex}} \sim 20 \text{ K}$ or higher.

We derive the total mass of each lobe by integrating over narrow velocity intervals assuming $T_{\text{ex}} = 20 \text{ K}$ and a CO/ H_2 ratio of 10^{-4} by correcting for the derived opacity as a function of velocity. We note that the opacity correction increases the mass estimates by ~ 2.6 for the blue outflow and by a factor of 1.5 for the red, resulting in total masses of $0.37 M_{\odot}$ and $0.15 M_{\odot}$ for blue- and redshifted gas, respectively. At low velocities the redshifted gas is hidden by the intense emission from the 10.5 km s^{-1} cloud component, and we are likely to miss a considerable fraction of the low-velocity gas (which also has the highest opacity correction). We obtain a dynamical timescale of $\sim 2500 \text{ yr}^{-1}$ for each lobe from the observed linear extent of the outflow and the maximum velocity for each outflow lobe, $160''$ and 110 km s^{-1} for the red outflow lobe and $130''$ and 90 km s^{-1} for the blue outflow lobe. These timescales are uncorrected for inclination. We also derive momentum (P), kinetic energy (E), mechanical luminosity (L_{mech}), and momentum flux (F_{CO}) of each outflow lobe by integrating over the observed CO emission. Since we apply no inclination correction, these quantities will be true lower limits to the actual values (see, e.g., Cabrit & Bertout 1992). The momenta of the flow are roughly equal in both flows (1.7 and $1.8 M_{\odot} \text{ km s}^{-1}$) for the blue- and redshifted outflow, respectively, while the kinetic energy (7.1 and $17.2 M_{\odot} \text{ km s}^{-1}$), the mechanical luminosity (0.06 and $0.23 L_{\odot}$) and the momentum flux ($3.3 \cdot 10^{-5}$ and $3.0 \cdot 10^{-3} M_{\odot} \text{ km s}^{-1} \text{ yr}^{-1}$) are much higher for the faster redshifted outflow. For computing the above properties of the outflow we have largely followed the methods outlined in Choi et al. (1993) and Cabrit, Goldsmith, & Snell (1988).

3.3. The Submillimeter Core

The position we deduce for NGC 2023 mm1— $\alpha(1950.0) = 2^{\text{h}}38^{\text{m}}53^{\text{s}}.8$, $\delta = -05^{\circ}19'35''.9 \pm 2''$ —differs by $\sim 10''$ from the position reported by Launhardt et al. (1996) (LBS 36 SM1) but refers to the same source, which is easily seen from the similarity in morphology and the

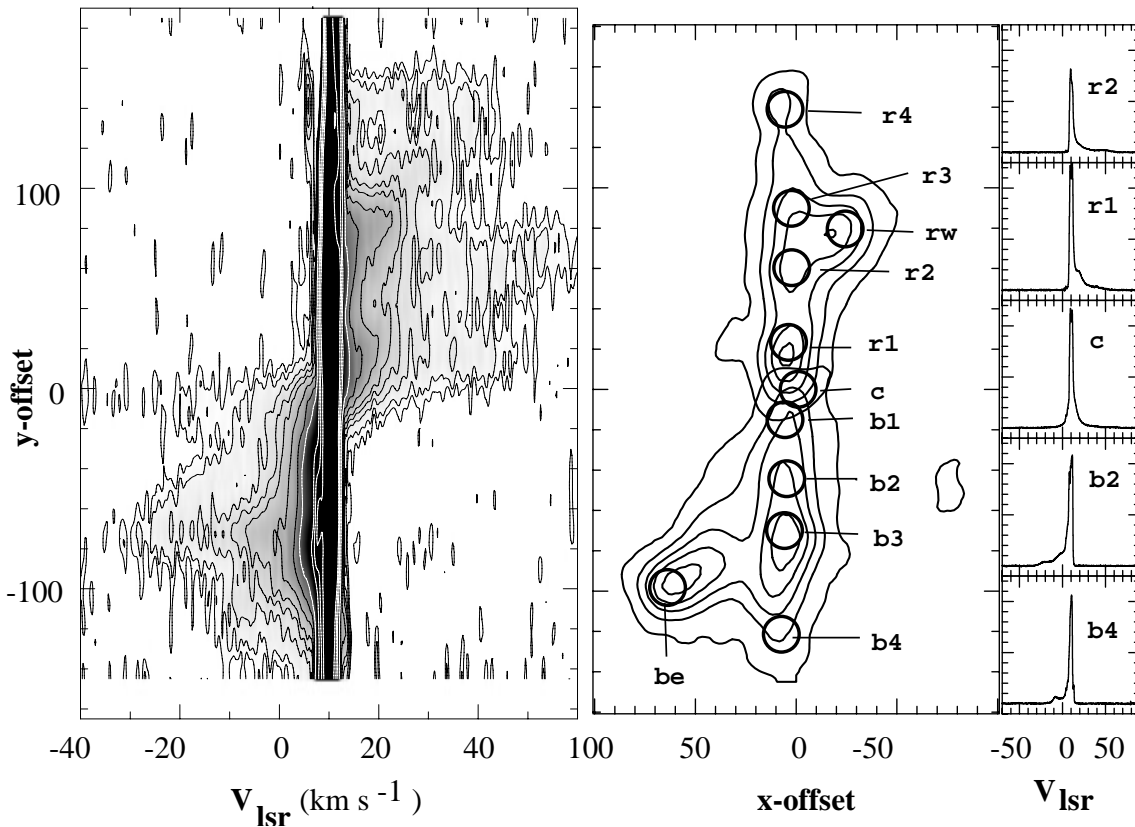


FIG. 5.—CO $J = 3 \rightarrow 2$ outflow rotated by -35° and integrated from -20 to $+7.5$ km s^{-1} in blue and from 13.5 to 50 km s^{-1} in red. The labeled circles mark hot spots in the outflow, as identified from channel maps in narrow velocity intervals. To the right the long-integration CO $J = 2 \rightarrow 1$ spectra are shown of selected positions, and on the left-hand side we show a velocity position plot obtained by integrating from $+15$ to $-10''$ in x . The units of the x - and y -offsets are in arcseconds, and V_{lsr} is given in km s^{-1} .

good agreement in flux density (Table 1). From the $450 \mu\text{m}$ map, which has the highest resolution, we derive a source size of about $5''.5$ ($6''.5 \times 4''.7$), close to the value quoted by Launhardt et al. (1996). The source appears slightly elongated, with a position angle of -42° at both 450 and $850 \mu\text{m}$. We identify this source as the star driving the outflow because it lies on the symmetry axis of the outflow and at the intersection of red- and blueshifted high-velocity gas (Fig. 4). The much fainter companion $\text{mm}2-\alpha(1950.0) = 2^{\text{h}}38^{\text{m}}55^{\text{s}}.14$, $\delta = -05^\circ 19' 47''.0 \pm 2''$ appears more extended, $\sim 3''.6 \times 7''.3$, with a position angle of -19° . It is connected to $\text{mm}1$ with a bridge of dust. There is a clear north-south ridge of dust emission, which is probably broader than seen in our SCUBA image because there is clear evidence that we were chopping onto emission in our off position. We find no obvious outflow activity from $\text{mm}2$, although both the CO $J = 2 \rightarrow 1$ and CO $J = 3 \rightarrow 2$ maps show an extended kinematic feature at about 15 km s^{-1} northeast of $\text{mm}2$, but we see no blueshifted counterflow to the southwest, and hence the redshifted lobe could just be an unrelated cloulet seen along the line of sight. A third faint, almost separate, emission region is seen to the south and is only partially covered by the SCUBA 850 and $450 \mu\text{m}$ maps.

Since our photometry of $\text{mm}1$ (Table 1) covers the whole submillimeter-wavelength regime, we can use this information to constrain the dust properties and the mass of $\text{mm}1$. If we assume that the dust grains can be characterized by a single dust temperature, T_d , where T_d would be the harmo-

nic mean of all dust grains along the line of sight, then the flux density S_ν at frequency ν can be written as

$$S_\nu = \Omega_s B_\nu(T_d)(1 - e^{-\tau_\nu}), \quad (1)$$

where Ω_s is the source solid angle, $B_\nu(T_d)$ is the Planck function, and τ_ν is the optical depth at ν . We write τ_ν as

$$\tau_\nu = \tau_o \left(\frac{\nu}{\nu_o} \right)^\beta, \quad (2)$$

where τ_o is the dust optical depth at frequency ν_o , and β is the dust emissivity index describing how the dust opacity ($\tau_\nu \propto \kappa_\nu$) changes as a function of frequency (see, e.g., Hildebrand 1983; Emerson 1988). It is now straightforward to do a least-squares fit to equation (1). Since we mapped the source, we can assume the source size to be known, and from our analysis of the molecular line data we can additionally constrain the dust temperature. The gas densities required to explain the observed dust emission are very high, $n \geq 10^7 \text{ cm}^{-3}$, and we can safely assume the dust grains to have the same temperature as the gas. We therefore know that the dust temperature is less than 40 K and probably closer to 20 K, the value derived from C^{18}O . If we correct the fluxes for a $5''$ source size and additionally constrain the dust temperature T_d to the above range, we obtain a $\beta = 1.06$ and a dust temperature $T_d = 24.3$ K with a total luminosity $L_{\text{bol}} \sim 6.8 L_\odot$. In this fit we have excluded the flux at 2 mm, since it appears too bright (see Fig. 6). At 2 mm the HPBW is $27''$, and it is therefore likely that some of

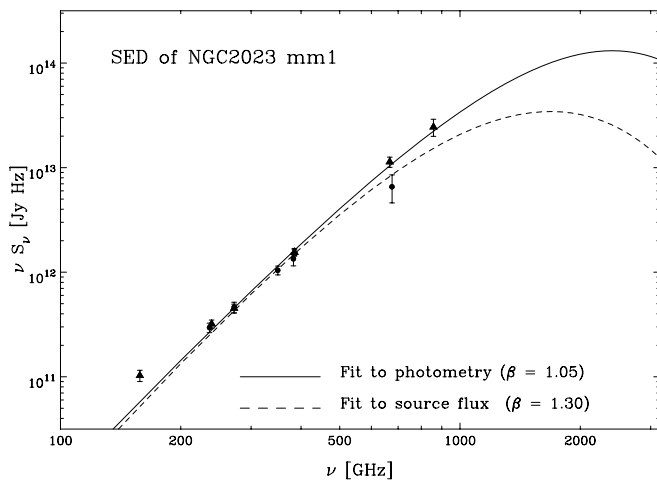


FIG. 6.—Spectral energy distribution for NGC 2023 mm1 as determined from (sub)millimeter photometry (i.e., source plus underlying cloud) (filled triangles) and by estimating the total flux of the source using Gaussian fits (filled circles). The solid curve illustrates a typical isothermal dust fit to photometry data, while the dashed curve is a more extreme fit to the total flux densities determined from map data. Note that none of the fits do a very good job at long wavelengths, and neither does the latter fit at 450 μm , which suggests either that there are problems with the calibration or that the data cannot be described by an isothermal model.

the flux is due to mm2 and the surrounding extended emission. Some of the 2 mm excess emission may also be due to free-free emission, most likely originating from a partially ionized jet. The temperature is largely arbitrary, because we have no FIR data to constrain the temperature. However, we cannot make the source too hot, because then it should have been seen by *IRAS*, yet *IRAS* HIREs data (see, e.g., Launhardt et al. 1996) show no sign of a source at the position of mm1 and mm2. If we constrain the fit to a dust temperature of 30 K, it hardly changes the β index ($\beta \sim 1.0$), but it doubles the bolometric luminosity. Our photometry data definitely exclude any β value over 1.4. This would require $\theta_s \lesssim 2''$, which is in conflict with our observational data that appear to resolve the source. For simplicity we adopt $T_d = 25$ K, which corresponds to $\beta = 1.05$ and which is the fit plotted in Figure 6. This corresponds to a total luminosity $L_{\text{bol}} \sim 7.6 L_\odot$. Assuming Hildebrand (1983) opacities ($\kappa_{1200 \text{ GHz}} = 0.1 \text{ cm}^2 \text{ g}^{-1}$) and a gas-to-dust ratio of 150, we derive a mass of $2.8 M_\odot$, far less than that derived by Launhardt et al. (1996), who used a temperature of 20 K and assumed $\beta = 2$. By using a priori assumptions about dust temperature and source size, we can seemingly derive relatively accurate dust masses. However, the absolute value of the dust opacity at 250 μm (1200 GHz) is poorly known, and literature surveys, e.g., Henning, Michel, & Stognienko (1995), report a spread of a factor of 10, depending on what dust model or method has been used to deduce the opacity.

Since we have maps at five wavelengths, if we include the data from Launhardt et al. (1996), we should actually be able to get a better estimate of the properties of mm1 from the maps rather than using photometry. The photometry data are as such more accurate than the maps and span a larger wavelength range, but they include a significant amount of emission from the surrounding molecular cloud core. If we plot the total fluxes estimated from fitting an elliptical Gaussian to mm1 (Fig. 6), we find that the map

data are consistently below the photometry points, as one would expect. However, the difference at 450 μm is surprisingly large. This discrepancy can partly be explained by calibration errors, but not entirely. If we smooth the 450 μm map to the same beam size as used for photometry, we get a peak flux of $16.4 \text{ Jy beam}^{-1}$, close to the observed photometry value. We would also expect to see a larger difference between photometry and true flux density at shorter wavelengths if the underlying molecular cloud core has a steeper spectrum than mm1. That this is indeed the case is verified by fitting a dust-emissivity law to the molecular cloud core (see below). Even so, the flux density derived for mm1 from the 450 μm map is likely to be an underestimate because it is rather difficult to fit the map data with realistic assumptions about the dust surrounding mm1. The fit we show in Figure 6 is reasonably good, but it forced the solution to our lower limit in temperature, $T_d = 20$ K, and required a source size, $\theta_s = 3''$, smaller than our previous limit. The fitted β value is in this case 1.3, but for these rather extreme assumptions the dust emission is already significantly optically thick in the millimeter range ($\tau_{1.3 \text{ mm}} \sim 0.3$). This would correspond to a mass of $4.6 M_\odot$ and a bolometric luminosity of $2.1 L_\odot$. However, since mm1 drives a very energetic outflow, a dust temperature of 20 K is rather unrealistic. We have therefore also fitted the data by requiring $T_d = 25$ K, and $\theta_s = 5''$, which results in $\beta = 1.02$, a mass of $1.8 M_\odot$, and a luminosity of $6.8 L_\odot$, which is close to what we obtained from photometry. In this case, however, the fit clearly overestimates the 450 μm data. This may simply suggest that the data cannot be fitted by a simple isothermal dust model. However, given the uncertainty in the data, we do not find it justified to try a more realistic model, e.g., a hotter inner core surrounded by a cooler envelope, which would certainly fit our data set much better.

For mm2 we have to rely on map data, and since mm2 is both fainter and more extended, it is difficult to separate the dust emission of mm2 accurately from that of the surrounding cloud. The best estimates of the total flux are 0.33 Jy at 1.3 mm (Launhardt et al. 1996) and $4.8 \pm 2.0 \text{ Jy}$ from our 450 μm map. These flux densities predict a β index of $\sim 1.04 \pm 0.3$, corresponding to a total mass of $0.6 \pm 0.3 M_\odot$ and a luminosity of $3 L_\odot$ for a dust temperature of 25 K.

It is difficult to estimate the total amount of dust associated with the molecular cloud core surrounding mm1 and mm2. The dust emission is more extended than the SCUBA field of view, and the UKT14 maps have a poor S/N ratio for the relatively faint extended emission. All maps, however, show a similar morphology close to the two submillimeter sources. This suggests that if we restrict our analysis to this core region, $\sim 40'' \times 65''$, we should not introduce too large errors. At 850 μm we derive an integrated flux of $1.5\text{--}3 \text{ Jy}$. The large uncertainties in this case result from our inability to assess an accurate flux value for mm2. At 450 μm we obtain $19 \pm 8 \text{ Jy}$, while Launhardt et al. quote a value of 0.5 Jy at 1.3 mm for a slightly smaller area. Our flux estimates are corrected for error lobe pickup, which at 850 μm adds about 15%–20% in integrated flux and at 450 μm almost a factor of 2 (80%). At 1.1 mm and 800 μm we obtain 1.2 ± 0.6 and $5.4 \pm 2.2 \text{ Jy}$, respectively. If we constrain the temperature to 20 K, which is more appropriate for a molecular cloud core, we obtain $\beta = 2$, which is the canonical value expected for normal interstellar dust grains (Hildebrand 1983). We note, however, that the errors in the integrated fluxes are large and the dust emiss-

ivity can certainly be lower than 2, but not much less than 1.7. If we adopt a $\beta = 2$, we derive a total luminosity of $6 L_{\odot}$ and a mass of the molecular cloud core of $7.5 M_{\odot}$.

4. DISCUSSION

4.1. NGC 2023 mm1: A Class 0 Source

André, Ward-Thompson, & Barsony (1993), in their study of the protostellar source VLA 1623, added a new group to the classification scheme of young stellar objects (YSOs) by Lada (1987) that more appropriately fits the characteristics of this extremely young protostellar source. This group, called class 0, represents the very youngest protostars, whose dense circumstellar envelopes or disks are more massive than the central hydrostatic protostellar core. Although there is not a clear cut distinction between class I (the youngest YSOs in Lada's classification scheme) and class 0 objects, all potential class 0 objects have large circumstellar envelopes or disks, are not detected in the visible or near-IR, and have generally been found in the FIR or submillimeter. Although most objects in this group do not directly show infall from the ongoing accretion, they appear to drive energetic and more collimated outflows than class I objects.

We classify the submillimeter source NGC 2023 mm1, which powers the jetlike outflow, as a class 0 source. Since the source powers a highly collimated bipolar outflow, it has already formed a stellar core. The spectral energy distribution is well fitted by a single temperature, although any submillimeter source completely lacking FIR and mid-IR data will in principle always be well fitted by a single temperature. From our submillimeter observations we deduce a β index in the range 1.0–1.3, a combined dust and gas mass of ~ 1.8 – $4.6 M_{\odot}$, and a luminosity of less than $15 L_{\odot}$ and more probably around $7 L_{\odot}$. The luminosity is rather uncertain because it depends on the temperature we assume for the dust, but our molecular line observations suggest that the dust core is unusually dense and cold. Integrating under our isothermal fits ($\nu \leq 900$ GHz), we derive a submillimeter-to-bolometric luminosity of greater than 3.0 times 10^{-2} , i.e., well within the range suggested by André, Ward-Thompson, & Barsony (1993): $L_{\text{submm}}/L_{\text{bol}} > 10^{-3}$. The low dust emissivity index follows the trend seen in other class 0 sources, which appear to have a low β index (Chandler 1998).

The outflow properties appear to be significantly different for class 0 objects compared to the more evolved class I sources. In general, the outflows from class 0 objects are more energetic and more highly collimated (see, e.g., VLA 1623, André et al. 1993; IRAS 4A, Blake et al. 1995; IRAS 2, Sandell et al. 1994; L1448 mm, Bachiller et al. 1990. Bontemps et al. (1996) reinvestigated the correlation between momentum flux (mechanical force) F_{CO} and bolometric luminosity L_{bol} and found a close correlation for class I sources, i.e., $F_{\text{CO}}/F_{\text{rad}} = 100$ (where $F_{\text{rad}} = L_{\text{bol}}/c$ is the radiative momentum flux), while they estimate that class 0 sources on average have outflow efficiencies about 10 times higher. For the NGC 2023 mm1 jet we derive an outflow

efficiency of 240, but we note that Bontemps et al. (1996) corrected their momentum flux for an average inclination of 57.3° and applied a higher opacity correction than we derived here. If we were to apply the same correction factors we would obtain ~ 1200 for the outflow efficiency, which is in good agreement with the average value they derive for class 0 sources.

4.2. A Jet-driven EHV Outflow?

Recent observational and theoretical modeling lend strong support to the idea that CO outflows are driven by highly collimated jets originating from the (proto)star powering the outflow (e.g., Masson & Chernin 1993; Raga et al. 1993, Chernin et al. 1994; Richer, Hills, & Padman 1992; Bence, Richer, & Padman 1996; Ouyed et al. 1997). The CO outflow from mm1 is very jetlike, especially at high velocities. A plot of CO velocity against distance (Fig. 5) shows a clear bow-shock signature, i.e., the highest velocities are seen at the tip of the outflow and the velocities decrease toward the central source, which is what one would expect from "prompt" entrainment by a high Mach number stellar jet. The outflow shows several peaks or hot spots, labeled as b1–b4 and r1–r4 in Figure 5, each tracing CO to extreme velocities with sharp leading edges, which suggests that they are bow shocks between a fast-moving jet and the surrounding ambient cloud. The outflow shows the same mirror-like symmetry as was seen in the IRAS 4A outflow (Blake et al. 1995) or in the RNO 43 superoutflow (Bence et al. Padman 1996), which suggests that it may be driven by a precessing jet. IRAS 4A is a binary (Lay, Carstrom, & Hills 1995), and in this case the jet precession could be explained by an interaction between the binary and the accretion disk.

The almost separate outflow lobes off the jet axis $\sim 100''$ from the source (labeled "be" and "rw" in Fig. 5) appear almost disconnected from the source, but at low velocities (especially in blue) we can see faint emission extending back to the source. These bow shocks can therefore be understood in terms of a wandering or precessing jet or as being caused by a sudden change in the jet direction. At a first glance the be/rw bow shocks would appear to be younger than the working surface of the main jet (r4/b4) because they are closer to the source, especially the slightly less pronounced lobe on the red side, which we labeled br. But the main jet has generally higher velocities than the be and rw hot spots, suggesting that this may be only an illusion. However, both an old and a young jet can be used to explain why we hardly see any high-velocity gas between the bow shock and the source. If the jet is very young, it will be underdense and almost all of the force will be applied to the working surface of the jet. If the jet is old, it could simply have cleared out the intervening gas between the bow shock and the source, and even if the jet is turned off, the bow shock continues to move forward because of its high initial momentum in a momentum conserving fashion (Bence et al. 1998).

REFERENCES

- André, P., Ward-Thompson, D., & Barsony, M. 1993, *ApJ*, 406, 122
 Bachiller, R., Chernicharo, J., Martín-Pintado, J., Tafalla, M., & Lazareff, B. 1990, *A&A*, 231, 174
 Bence, S. J., Padman, R., Isaak, K. G., Wiedner, M. C., & Wright, G. S. 1998, *MNRAS*, 299, 965
 Bence, S. R., Richer, J. S., & Padman, R. 1996, *MNRAS*, 279, 866
 Blake, G. A., Sandell, G., van Dishoeck, E. F., Groesbeck, T. D., Mundy, L., & Aspin, C. 1995, *ApJ*, 441, 689
 Bontemps, S., André, P., Terebey, S., & Cabrit, S. 1996, *A&A*, 311, 858
 Cabrit, S., & Bertout, C. 1992, *A&A*, 261, 274
 Cabrit, S., Goldsmith, P. F., & Snell, R. L. 1988, *ApJ*, 334, 196

- Chandler, C. J. 1998, in ASP Conf. Ser. 148, *Origins*, ed. C. E. Woodward, J. M. Shull, & H. A. Thronson (San Francisco: ASP), 237
- Chernin, L., Masson, C., Gouveia Dal Pino, E. M., & Benz, W. 1994, *ApJ*, 426, 204
- Choi, M., Evans, N. J., II, & Jaffe, D. T. 1993, *ApJ*, 417, 624
- Duncan, W. D., Robson, E. I., Ade, P. A. R., Griffin, M. J., & Sandell, G. 1990, *MNRAS*, 243, 126
- Emerson, J. P. 1988, in *Formation and Evolution of Low Mass Stars*, ed. A. K. Dupree & M. T. V. T. Lago (NATO ASI, Ser. C) (Dordrecht: Reidel), 193
- Henning, Th., Michel, B., & Stognienko, R. 1995, *Planet. Space Sci.*, 43, 1333
- Hildebrand, R. H. 1983, *QJRAS*, 24, 267
- Holland, W. S., Gear, W. K., Lightfoot, J. F., Jenness, T., Robson, E. I., Cunningham, C. R., & Laidlaw, K. 1998, in *Proc. SPIE* 3357, 305
- Lada, C. J. 1987, in *IAU Symp. 115, Star-Forming Regions*, ed. M. Peimbert & J. Jugaku (Dordrecht: Reidel), 1
- Lada, E. A., Bally, J., & Stark, A. A. 1991, *ApJ*, 368, 432
- Launhardt, R., Mezger, P. G., Haslam, C. G. T., Kreysa, E., Lemke, R., Sievers, A., & Zylka, R. 1996, *A&A*, 312, 569
- Lay, O. P., Carlstrom, J. E., & Hills, R. E. 1995, *ApJ*, 452, L73
- Masson, C. R., & Chernin, L. M. 1993, *ApJ*, 414, 230
- Ouyed, R., Pudritz, R. E., & Stone, J. M. 1997 *Nature*, 385, 409
- Raga, A. C., Cantó, J., Calvet, N., Rodriguez, L. F., & Torelles, J. M. 1993, *A&A*, 276, 539
- Richer, J. S., Hills, R. E., & Padman, R. 1992, *MNRAS*, 254, 525
- Sandell, G. 1994, *MNRAS*, 271, 75
- . 1999, in preparation
- Sandell, G., Knee, L. B. G., Aspin, C., Robson, I. E., & Russell, A. P. G. 1994, *A&A*, 285, L1